



Controllable synthesis of substitutional and interstitial nitrogen-doped ceria: The effects of doping sites on enhanced catalytic ozonation of organic pollutants

Shujuan Zhan^a, Huating Huang^a, Chun He^{a,b}, Ya Xiong^{a,b}, Ping Li^{a,b,*}, Shuanghong Tian^{a,b,*}

^a School of Environmental Science & Engineering, Sun Yat-sen University, Guangzhou 510275, PR China

^b Guangdong Provincial Key Laboratory of Environmental Pollution Control and Remediation, PR China

ARTICLE INFO

Keywords:

Nitrogen-doped ceria
Interstitial N
Substitutional N
Catalytic ozonation
DFT calculations

ABSTRACT

Nitrogen doping sites greatly affected the electronic structure of catalysts. However, identification of nitrogen doping sites in CeO₂ and their effects on catalytic ozonation have never been addressed. Herein, nitrogen was selectively doped at substitutional (N_s) or interstitial sites (N_i) in CeO₂ by simply controlling the heat treatment conditions. The obtained N-Ce2-400 with 100% N_i significantly enhanced the elimination of sulfamethoxazole to 93.7 ± 1.9% within 30 min at the initial solution pH of 6.2. The first-order rate constant reached 8.77 × 10⁻² min⁻¹, 2.1 and 4.1 times that of 50.1%N_s-doped CeO₂ and ozonation, respectively. The experimental and DFT calculation results demonstrate that compared to N_s, N_i favors the formation of oxygen vacancies (OVs). Both N_i and OVs significantly decreased the energy barrier of the adsorption and activation of ozone. This study provides a simple site-tunable N-doping method and gains a new insight into the roles of N_i and N_s in catalytic ozonation.

1. Introduction

Pharmaceuticals and personal care products (PPCPs) have been widely consumed throughout the whole world [1,2]. Due to their high applicability and stability, PPCPs have been extensively detected in aquatic environment, leading to persistent pollution [3,4]. Advanced oxidation processes (AOPs), e.g., catalytic oxidation, photocatalysis, catalytic ozonation, are often adopted for the degradation of PPCPs due to the formation of reactive oxidation species (ROS), e.g., non-selective hydroxyl radicals [5,6]. Among them, catalytic ozonation has been regarded as one of the most effective and environmental benign technologies operated under mild conditions. Particularly, compared to catalytic oxidation and photocatalysis, catalytic ozonation has the advantages of wide adaptability to pollutant types and concentrations, high oxidation efficiency, as well as low reaction temperature and normal operation pressure [7–10]. In catalytic ozonation process, solid catalysts can accelerate the decomposition of ozone into highly reactive oxygen species (ROS). This promotes the dissolution of gaseous O₃ and thus decreases O₃ wastage. In the meanwhile, the produced ROS with high oxidability can destroy the refractory pollutants and their toxic intermediates that cannot be oxidized by ozone alone [11–13]. Therefore, the development of effective and robust ozone catalysts has become

the key of heterogeneous catalytic ozonation technology.

Ceria, due to its high oxygen storage capacity, abundant oxygen vacancies and reversible Ce³⁺/Ce⁴⁺ redox pair, has been extensively applied in many catalytic reactions such as water-gas shift [14–17], CO oxidation [18–20], soot combustion [21–24], selective catalytic reduction of NO_x [25–27], photocatalysis [28,29], and catalytic ozonation [30,31]. Especially in catalytic ozonation, ceria or modified ceria has an outstanding characteristic that it can simultaneously enhance the degradation of organic pollutants and inhibit the formation of potential carcinogen bromate when treating the Br⁻ containing water such as seawater, ground water and so on [30]. To furthermore improve the catalytic activity of ceria, research on modifying its crystal lattice and electronic structure has attracted a great deal of attention. Many literatures have proved that doping heteroatoms into ceria is a significantly effective method. Heteroatom doping can be classified as cationic (e.g., Mn, Fe, Ag) doping [31–34] and anionic (e.g., N, S, F) doping [35–37]. Among them, N doping is considered as a viable method to tune the electronic structure and performance of ceria because of its similar ionic radius, electronegativity, electronic polarizability to oxygen (O) [38]. With the introduction of N into CeO₂, the 2p orbital of N can mix with the 2p orbital of O for the alteration in the electronic band structure [39]. According to the current reports, doping nitrogen into the lattice of

* Corresponding authors at: School of Environmental Science & Engineering, Sun Yat-sen University, Guangzhou 510275, PR China.

E-mail addresses: liping56@mail.sysu.edu.cn (P. Li), tshuangh@mail.sysu.edu.cn (S. Tian).

<https://doi.org/10.1016/j.apcatb.2022.122040>

Received 21 June 2022; Received in revised form 25 August 2022; Accepted 1 October 2022

Available online 4 October 2022

0926-3373/© 2022 Elsevier B.V. All rights reserved.

the ceria could be implemented by hydrothermal-calcination [40,41], biotemplates-mediated calcination [42], hydrothermal treatment with the assistance of deep eutectic solvent [43], solvothermal treatment [44], and ion beam assisted deposition methods [45]. It can be seen that doping ceria with anions of N is not easy compared to doping with cations, and often requires harsh conditions or special means. However, the obtained N-CeO₂ showed excellent catalytic activity not only for visible light-driven photocatalysis [41–44], but also for many other areas of non-photo catalysis, e.g., selective catalytic reduction of NO with NH₃ [40] and catalytic hydrogenation of phenylacetylene [46]. Usually, the origin of the enhanced catalytic activity of N-doped ceria was ascribed to the narrowed bandgap energy, improved plasmonic properties, and the rich defects of oxygen vacancies (OVs) and Ce³⁺ species in the ceria. Due to the similar atomic size of N to that of O, it has been proved that in N-doped TiO₂ and MnO₂, there are two kinds of nitrogen with two different doping sites, namely interstitial N (N_i) and substitutional N (N_s). When the N atom is inserted into the interstitial site of the lattice and constitutes Ti-N-O or Mn-N-O, these nitrogen species are called interstitial N (N_i). In contrast, the N atoms that replace lattice oxygen or occupy oxygen vacancies to form Ti-N-Ti or Mn-N-Mn are called substitutional N (N_s). N_i and N_s in TiO₂ and MnO₂ showed significantly different internal regulation of the atomic and electronic structure, and therefore imposed greatly influence on the catalytic reactivity. However, to the best of our knowledge, the concept of N_i and N_s in N-doped CeO₂ has never been distinguished, let alone further identification of the doping sites and investigation of their effects on catalytic activity. Moreover, N-doping inevitably produced OVs [40,47]. Studies have well proved that the introduction of OVs can significantly boost the catalytic performance of CeO₂ in catalytic ozonation [31]. Therefore, it is also interesting to explore the effects of N_i or N_s on the formation of OVs, and the effects of coexistence of OVs and N_i or N_s on tuning the atomic and electronic structure of ceria and their catalytic performance in catalytic ozonation.

In this work, we developed a facile urea-assisted heat treatment method to prepare N-doped ceria with tunable doping sites (N_i and N_s) and demonstrated their catalytic performance and mechanism for ozonation of organic pollutants. Four aspects of this research would be focused on: (1) to controllably synthesize N-doped ceria by a facile urea-assisted heat treatment method; (2) to identify the nitrogen doping sites and the resulting oxygen vacancies in N-doped CeO₂; (3) to investigate the catalytic performance of the N_i and N_s-doped ceria; (4) to reveal the catalytic mechanism by both experiments and density functional theory (DFT) calculations. In particular, the effects of N_i and N_s on the formation energy of OVs, the atomic and electronic structure of CeO₂, as well as the adsorption and decomposition of ozone on N-doped ceria were atomically investigated. The goal of this work is to provide a facile method to prepare N-doped ceria with tunable doping sites (N_i and N_s), and a deeper understanding the effects of N doping sites on the atom structure and catalytic performance of N-doped ceria.

2. Experimental

2.1. Materials

Cerium (III) nitrate hexahydrate, sodium hydroxide, 5,5-dimethyl-1-pyrroline N-oxide (DMPO), dimethyl sulfoxide (DMSO), 2,2,6,6-tetramethylpiperidine (TEMP), benzoquinone (p-BQ) and sulfamethoxazole (SMZ) were bought from Aladdin Chemistry Co., Ltd. (China). Urea, tert-butyl alcohol (TBA) and furfuryl alcohol (FA) were obtained from Tianjin Baishi Chemical Reagent Co., Ltd. (China). All chemicals were of analytical grade and used without further purification. The water used throughout all the experiments was purified through a Millipore system.

2.2. Preparation of catalysts

2.2.1. Preparation of Ceria

For the synthesis of ceria, 1.3 g of Ce(NO₃)₃·6H₂O and 14.4 g of NaOH were dissolved in 20 and 40 mL of deionized water, respectively. Then two solutions were mixed and then kept for stirring for 30 min. The resulting solution was transferred into a Teflon-lined stainless-steel autoclave and hydrothermally treated at 100 °C for 24 h. The formed solids were separated by centrifugation and washed with deionized water and ethanol several times, and dried in an oven at 80 °C for 8 h.

2.2.2. Preparation of N-doped ceria

N-doped ceria was prepared by a facile heat treatment with urea as nitrogen source under Argon atmosphere. As shown in Fig. 1a, the porcelain ark containing urea was placed in the first half of the porcelain ark that containing pure ceria. By controlling the mass ratios of ceria/urea at 4:1, 2:1 or 1:1 and the heat treatment at 400 °C, 500 °C, or 600 °C for 10 min, a series of N-doped ceria samples were obtained. They were designated as NCe-x-y (x = 4, 2, 1, y = 400, 500, 600), where x means the mass ratio of ceria/urea and y represents the treatment temperature. Totally five samples were obtained, i.e., NCe4-400, NCe2-400, NCe1-400, NCe2-500 and NCe2-600. As a control sample, CeO₂ was obtained by treating the pure ceria at 400 °C for 10 min in the absence of urea.

2.3. Characterization

XRD patterns of all the samples were performed on a D/MAX 2200 VPC diffractometer (Rigaku Corporation, Japan) with the Cu Kα radiation at 40 kV and 40 mA. Their morphologies were observed by a high-resolution transmission electron microscope (HRTEM, JEM-2010HR, JEOL) operated at 200 kV. X-ray photo-electron spectroscopy (XPS) of the samples were conducted with an ESCALAB 250, Thermo-VG Scientific (UK) system. The specific BET surface area of the samples was measured by N₂ physical adsorption at 77 K using an auto-adsorption system (Autosorb-6, Quanta chrome). Autosorb-iQ (Quantachrome Instruments, USA) was used to analyze the hydrogen temperature-programmed reduction (H₂-TPR) of the samples. Their Raman spectra were collected on Renishaw InVia Raman microscope with the laser length of 514 nm. Electron spin resonance (ESR) spectra of both the radicals in the solution and the ceria powder were measured with a Bruker EMXnano system. Cyclic voltammetry (CV) measurements for the samples were performed using an CHI760E electrochemical workstation (Zahner, Germany) with a standard three-electrode assembly.

2.4. Analysis methods

The concentration of SMZ was quantified by high performance liquid chromatography (HPLC) instrument (Shimadzu LC-15 C) with a UV detector set at 265 nm (Wondasil C18 column, 4.6 × 150 mm, particle size of 5 μm). The total organic carbon (TOC) was determined by a TOC analyzer (Shimadzu, Japan). The concentration of gaseous ozone was continuously monitored with an online ozone analyzer (IDEAL-2000, IDEAL tech Inc. China).

2.5. Catalytic ozonation procedures

Catalytic ozonation was carried out in a 100 mL glass column reactor in semi-batch mode. Ozone produced by an ozone generator (YE-TG-01PII, Nanjing YDG ozone Co., Ltd., China) with a concentration of 1 mg/L and a flow rate of 200 mL/min was bubbled into the bottom of reactor through a ceramic aeration head. The residue ozone from the system was quenched by passing through KI solution before their release to the air. For each run, the reactor was charged with 50 mL of wastewater containing 50 mg/L of SMZ and 0.03 g of catalysts. The natural pH of SMZ-containing solution is about 6.2, which is not controlled any

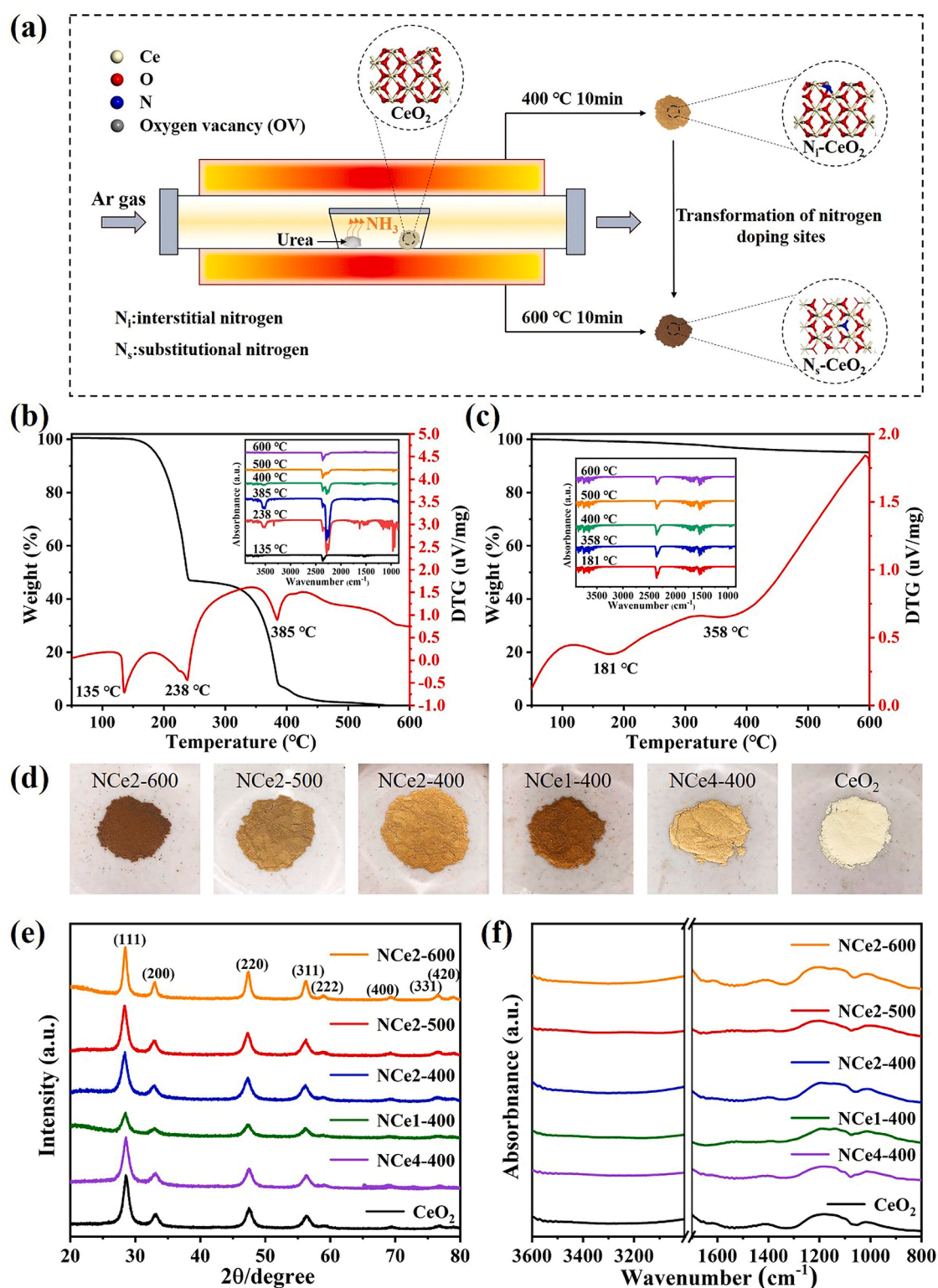


Fig. 1. (a) Schematic diagram of the controllable synthesis of N-doped ceria, TGA-IR curves of (b) urea and (c) N-Ce2-400, (d) photographs, (e) XRD patterns and (f) FTIR spectra of the ceria catalysts.

more during the following oxidation. The reaction mixture was continuously stirred by a magnetic stirrer and the temperature was controlled at around 25 °C by the recirculated cooling water around the reactor. At fixed intervals, 1 mL of aqueous sample was taken from the reactor and immediately purged with N_2 to remove the residual ozone. Then the sample was passed through a 0.22 μm filter membrane and analyzed for various purpose. As a control experiment, ozonation was also performed

with the same procedure except that no catalyst was loaded in the reactor.

2.6. Computational methods

The first-principle density functional theory (DFT) calculations were carried out using the Vienna ab initio simulation package (VASP). The

projector augmented plane-wave method was used to represent the core-valence interaction [48–51]. The generalized gradient approximation (GGA) was used for the exchange correlation function in the formulation of Perdew-Burke-Ernzerh (PBE) [50]. The DFT +U method with a U value of 5.0 eV was adopted for the highly localized Ce 4 f states in both undoped and doped ceria [49]. The cutoff energy of 420 eV and the Brillouin zone of a $2 \times 2 \times 2$ k-points mesh were applied for geometry optimization. The convergence of energy criterion and the force threshold was set as 10^{-5} eV and 0.02 eV/Å, respectively. A 5-layer CeO₂ (110) slab model was constructed with the bottom 2 layers fixed to simulate ozone on the CeO₂ surface. In the slab model, the vacuum thickness was set as 15 Å to separate each slab [52]. The transition state of the activation of ozone on the surface of N-doped ceria were searched with the climbing image nudged elastic band (CINEB) approach [53,54]. The saddle points were furthermore confirmed by only one imaginary frequency.

3. Results and discussion

3.1. Controllable synthesis of N-doped ceria

Herein N-doped ceria was prepared by a facile heat treatment with urea as nitrogen source under Argon atmosphere. As shown in Fig. 1a, during the heat treatment, urea was placed in a separate porcelain ark in front of that containing the pristine ceria. As indicated by the TGA results of urea in Fig. 1b, two endothermic peaks at 135 °C and 238 °C were attributed to the water evaporation and the decomposition of urea, respectively, and the third endothermic peak at 385 °C was ascribed to the further decomposition of intermediates [55]. The FTIR of the gas released from the decomposition of urea at various temperature was shown in the inset of Fig. 1b. At 238 °C, there appeared a weak double peak at around 3550 cm⁻¹, which is resulted from the stretching vibration of NH₃. The intensity of this peak is linked to NH₃ concentrations. This peak became stronger with the increase of the thermal temperature to 385 °C and almost disappeared over 400 °C. It indicates that the real dopant is NH₃ released from decomposition of urea as designed. Below 400 °C, N-doping continuously occurred by the interaction of NH₃ with CeO₂. After that, no more NH₃ was released and certainly the N-doping reaction stopped. The thermal behavior of N-Ce2-400 is also investigated and shown in Fig. 1c, slight mass loss occurred in the temperature range from 400 °C to 600 °C, which is probably due to the release of lattice oxygen and some nitrogen. The peak of DTG is possibly resulted by the phase transformation or crystallized CeO₂ [56].

It is obvious that nitrogen doping will greatly depend on the doping temperature and the mass ratio of ceria/urea (the amount of urea). The photographs of the ceria samples treated at various temperature and mass ratio of ceria/urea were shown in Fig. 1d. By fixing the doping temperature at 400 °C, pure CeO₂ is light yellow. The color became deeper with the decrease of the mass ratio of ceria/urea in the order of CeO₂ (1:0) < N-Ce4-400 (4:1) < N-Ce2-400 (2:1) < N-Ce1-400 (1:1). It is deduced that N-doping more seriously occurred when the relative amount of urea increased. As discussed above, no nitrogen doping and no obvious weight loss occurred above 400 °C. However, the increase of thermal treatment temperature from 400 to 600 °C obviously deepened the color from the sand yellow color of N-Ce2-400 to the brown color of N-Ce2-600. It implies that something other than nitrogen doping must have happened to the N-doped sample under the thermal treatment of above 400 °C. To reveal it, the phase of the ceria samples was further investigated by XRD. As shown in Fig. 1e, all the samples displayed eight diffraction peaks at 28.56°, 33.18°, 47.46°, 56.24°, 59.06°, 69.38°, 76.62° and 79.68°, which belongs to the (111), (200), (220), (311), (222), (400), (331) and (420) crystal planes of the cubic fluorite CeO₂ (JCPDS no. 43-1002), respectively. No impurity peaks of nitrogen-containing compounds or other ceria phase were observed possibly due to the low doping level or the high dispersion of new species.

Moreover, there was no evident change in the XRD peak position of ceria after heat treatment in the presence of urea. At the fixed 2:1 mass ratio of pristine ceria to urea, the heat treatment at 400 °C or even 500 °C did not obviously change the peak intensity of N-Ce2-400 and N-Ce2-500 in comparison with the pure CeO₂ treated at 400 °C in the absence of urea. It implies that the thermal treatment above 400 °C did not deteriorate the crystallinity. Until the temperature increased to 600 °C, the intensity of the peaks became much stronger. It indicates that the crystallinity of N-Ce2-600 increased significantly. At the fixed heat treatment temperature of 400 °C, with the decrease in mass ratio of ceria/urea from 4:1 to 1:1, more urea was applied, which resulted in the release of more NH₃ and thereof heavier N-doping. Especially in the case of N-Ce1-400, the heavy N-doping led to the obvious loss of crystallinity in comparison with pure CeO₂. It furthermore suggests that N atoms were successfully doped into the CeO₂ lattice below 400 °C [41]. Fig. 1f depicted the FTIR spectra of the ceria and N-doped ceria samples, no peaks of NH₂, NH₃ or NH₄⁺ were observed in the FTIR spectra. In Fig. S1, the adsorption-desorption isothermal curves of CeO₂ and N-doped CeO₂ were displayed. Both curves present a typical IV isotherm. The results of specific BET surface area (S_{BET}) were shown in Table 1. Compared to the S_{BET} of CeO₂, that of N-Ce2-400 and N-Ce4-400 slightly increased while that of N-Ce2-500 and N-Ce2-600 slightly decreased. However, no remarkable differences were observed between undoped and N doped catalysts.

TEM images, HRTEM images, and EDS elemental mapping of the pristine CeO₂ and N-doped CeO₂ are presented in Fig. 2. All the samples were composed of nanorods with a diameter of 4–12 nm and a length of 40–150 nm (Fig. 2a, d, g). It indicates that N-doping did not obviously change the morphology and crystal size of the ceria. The HRTEM images in Fig. 2b, e, h show that all the samples have the same lattice distance of 0.19 nm, which corresponds to the (110) plane of ceria. EDS elemental mapping unveils the distribution of N element on each sample. For the pristine CeO₂, only Ce and O were observed on the surface of the whole sample (Fig. 2c). In contrast, N were evenly distributed on the whole N-Ce2-400 like Ce and O (Fig. 2f). When the doping temperature furthermore increased to 600 °C, the obtained N-Ce-600 presented a lower density of N in comparison with N-Ce2-400 (Fig. 2i). The N amount of each sample was then quantified by EDS mapping and displayed in Table 1, there were 0.0 wt%, 2.1 wt% and 1.9 wt% for CeO₂, N-Ce2-400 and N-Ce2-600, respectively. N-Ce2-600 has a slightly lower N content than N-Ce2-400 because a few N atoms spilled out at high temperature like lattice oxygen [57,58].

3.2. Identification of the nitrogen doping sites and the resulting oxygen vacancies in N-doped CeO₂

Except the change of visual color, crystallization and S_{BET}, what else happened to N-doped ceria under the heat treatment above 400 °C? To further reveal the nitrogen doping sites and the concentrations of oxygen vacancies, the XPS spectra of CeO₂ and N-doped CeO₂ were achieved and analyzed. Fig. 3 presents the characteristic spin-orbit split of N 1 s, O 1 s, and Ce 3d signals of these samples. Only noise peaks are observed on CeO₂ while additional N 1 s signals existed in all the N-doped ceria at around 398 eV, which demonstrates again that N atoms were successfully incorporated into CeO₂. Moreover, obvious differences are observed in the N 1 s spectra of the samples treated at various temperature and mass ratio of ceria/urea. As shown in Fig. 3a, the N-doped sample of N-Ce2-600 prepared at the heat treatment temperature of 600 °C with the ceria/urea ratio of 2:1 showed an obvious N 1 s peak located at 396.5 eV (green peak), which is assigned to the formation of Ce-N bonds [42,59–61]. Actually, the binding energies in the 396–397 eV range ascribed to metal-N bonds have been widely observed and reported in N-doped TiO₂, TiN, and many other nitrides of transition metals [62–64]. The Ce-N bonds are formed by N substituting O or occupying oxygen vacancies in the lattice of CeO₂. Such N atoms were called substitutional N (N_s).

Table 1
Surface area and XPS results of the ceria catalysts.

Samples	S_{BET} (m^2/g)	N^{a} (%)	XPS				
			$\text{N}_{\text{Total}}^{\text{b}}$ (%)	$\text{N}_{\text{i}}/\text{N}_{\text{Total}}^{\text{c}}$ (%)	$\text{N}_{\text{s}}/\text{N}_{\text{Total}}^{\text{d}}$ (%)	$\text{OVs}/\text{O}_{\text{Total}}$ (%)	$\text{Ce}^{3+}/(\text{Ce}^{3+}+\text{Ce}^{4+})$ (%)
NCe2-600	55.2	1.9	1.3	49.9	50.1	22.0	24.1
NCe2-500	61.5	–	1.7	60.5	39.5	22.6	26.0
NCe2-400	72.0	2.1	1.8	100	–	24.5	30.1
NCe1-400	45.8	–	2.1	89.3	10.7	23.1	26.1
NCe4-400	82.1	–	1.1	100	–	20.6	23.9
CeO_2	68.3	0.0	–	–	–	19.8	18.8

Note: ^a The total N content is calculated from EDS elemental mapping. ^b The total N content is calculated from XPS results. ^c The relative content of interstitial N (N_{i}) to the total nitrogen is calculated from XPS results. ^d The relative content of substitutional N (N_{s}) to the total nitrogen is calculated from XPS results. The above values of N content are all mass fractions.

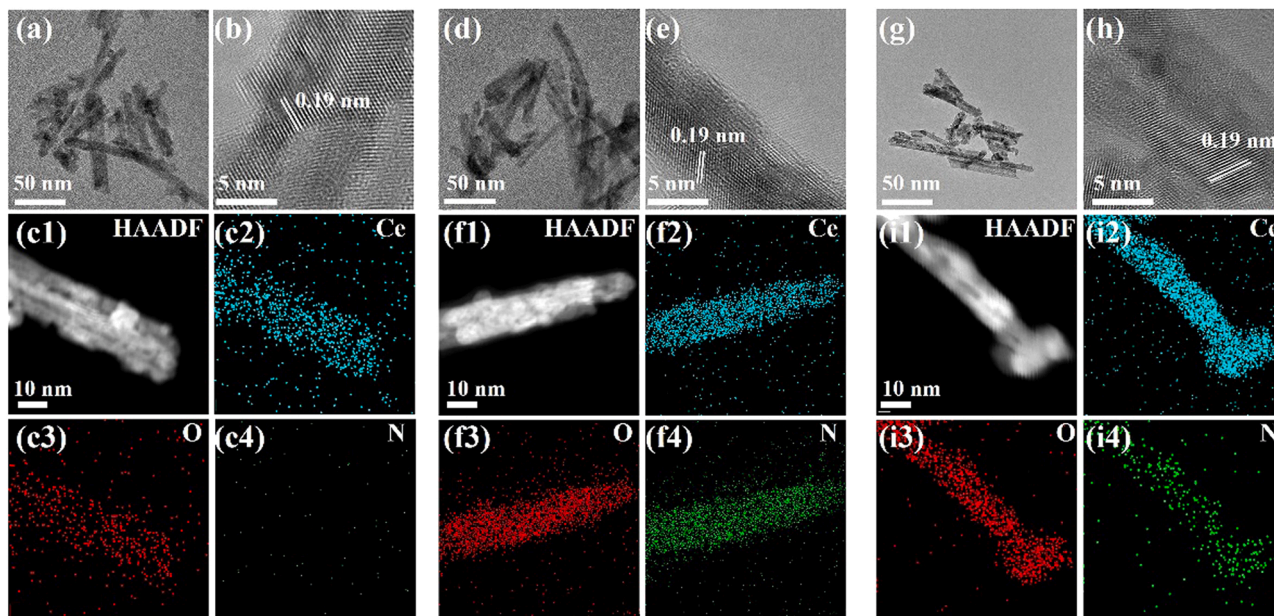


Fig. 2. TEM images, HRTEM images and EDS elemental mapping images of (a-c) CeO_2 , (d-f) NCe2-400 and (g-i) NCe2-600.

In addition, another peak with the comparable intensity to that of N_{s} was located at ~ 399.0 eV. Although N_{i} peak at about 396.5 eV or 399.0 eV of N-doped CeO_2 have been previously observed [35,40,42, 43], they have been totally assigned to the Ce-N without distinction. It is obviously not the fact since the difference in binding energy between 396.5 eV or 399.0 eV reaches as high as 2.5 eV. In other words, the nitrogen located at 396.5 eV and 399.0 eV have a completely different chemical environment. According to the literature [60], when CeO_2 coexists with CeN, apart from the peak around 396.2 eV caused by the Ce-N bond, another peak at higher binding energy at 398.2 eV was also observed, which might be originated from N-O bonds. Moreover, it is also reported that N_{i} peak at ~ 399.6 eV is ascribed to Ti-N-O in N-doped TiO_2 and to Mn-N-O in N-doped MnO_2 [47,62]. Therefore, it is believed that the peak at ~ 399.0 eV of N-doped ceria could belong to the characteristic peak of interstitial N (N_{i}), namely inserted into interstitial sites and directly connected to lattice oxygen (Ce-N-O). In order to eliminate the interference of N-H or absorbed NH_3 , whose binding energy is also closed to 399 eV, the results of FTIR (Fig. 1f) in the previous discussion were analyzed again. In Fig. 1f, no stretching or bending vibration peaks belonging to N-H or NH_3 were observed. Moreover, the peak of NO_x is located at a higher binding energy (>399 eV), which did not appear in the XPS spectra of Fig. 3a. Therefore, the peak at ~ 399 eV can be solidly regarded to be the characteristic peak of N_{i} . To the best of our knowledge, this is the first time that N_{i} and N_{s} in N-CeO₂ were clearly identified and distinguished. When the heat treatment temperature decreased to 500 °C, the obtained NCe2-500 also

showed such two peaks. However, the N_{s} peak became much weaker, and the intensity of the N_{i} peak obviously surpassed that of N_{s} . Different from the XPS spectra of NCe2-500 and NCe2-600, it is interesting to observe from the XPS spectra of NCe2-400 that the N_{s} peak totally disappeared and only a single N_{i} peak at ~ 399.0 eV remained. It demonstrates that compared to N_{s} , N_{i} easily formed at lower heat treatment temperature and the heat treatment above 400 °C probably made the transformation of N_{i} to N_{s} . Such transformation did not destroy the lattice of ceria but might arise the change of visual color and electronic structure.

According to the XPS results, the total N content (N_{Total}) and the relative content of N_{i} and N_{s} to N_{Total} were summarized in Table 1. The N_{Total} of NCe2-400 was 1.8 wt%, which is 100% N_{i} and closed to that determined by EDS. However, only 1.3 wt% N was detected in NCe2-600, substantially less than that determined by EDS. It can be partly explained by the high proportion of N_{s} (50.1%) in NCe2-600. Some studies have disclosed that N_{i} tends to be distributed on the shallow surface, whereas N_{s} generally resides in the bulk interior [65, 66]. Since XPS is a shallow surface detection technology in comparison with EDS, the N_{s} distributed inside ceria is not easily examined, resulting in much less N content than that detected by EDS technique. And the relative content of N_{i} in NCe2-500 and NCe2-600 decreased to 60.5% and 49.9%, respectively. Apparently, as the temperature increases, the relative content of N_{i} decreases due to the gradual transformation from N_{i} to N_{s} . This transformation was also found in N-doped TiO_2 [37].

Except the heat treatment temperature, the amount of nitrogen

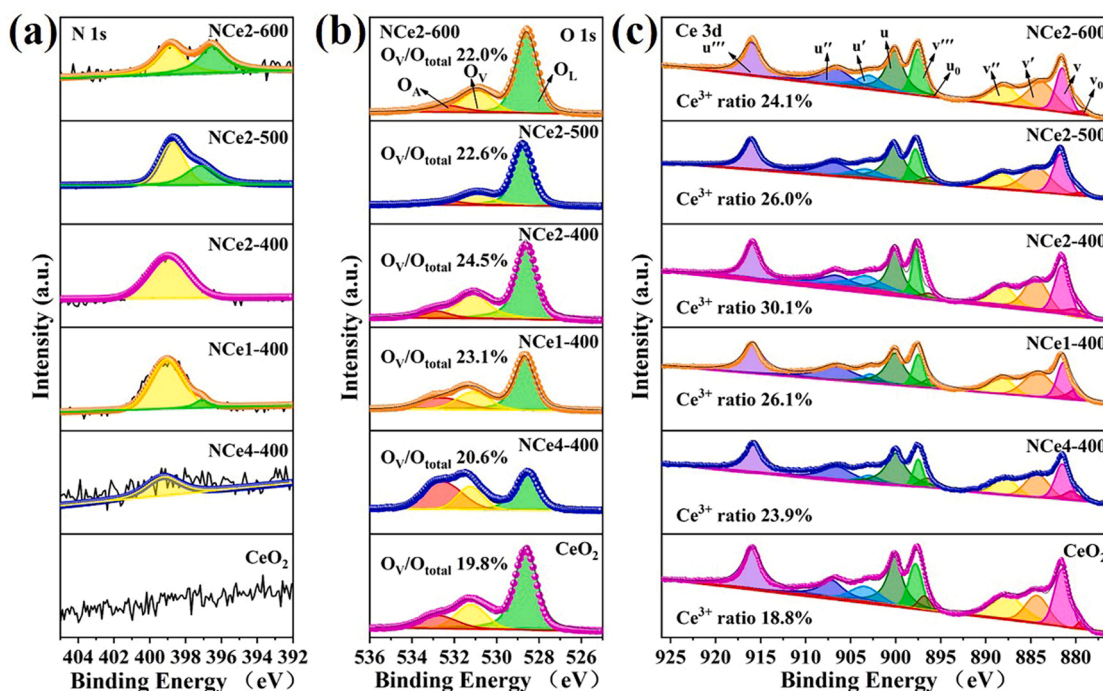


Fig. 3. XPS spectra of (a) N1s, (b) O1s and (c) Ce3d of the ceria catalysts.

source (urea) might also be another factor to control N doping sites and contents. The dosage of urea for the synthesis of NCe4-400 and NCe1-400 is half and twice that of NCe2-400, respectively. As shown in Fig. 3a and Table 1, in the case of NCe1-400, a very weak N_s peak appeared beside the strong N_i peak, which is 10.7% and 89.3% of the total doped nitrogen, respectively. In contrast, with the increase in mass ratio of ceria/urea to 4:1, the obtained NCe4-400 had a single weaker N_i peak and did not present any N_s peak. The N_i (or N_{total}) in NCe4-400 is only 1.1%, much less than that (1.8%) in NCe2-400 obtained at the ceria/urea mass ratio of 2:1. It demonstrates that at 400 °C, nitrogen atoms were preferentially doped to the interstitial sites. In the case of insufficient nitrogen source, only N_i -doping occurs. When the interstitial sites become saturated in the presence of adequate nitrogen source, the remaining N atoms would occupy oxygen vacancies or replace lattice oxygen atoms to form N_s .

In conclusion, both N_s and N_i may exist in N-doped CeO_2 and the nitrogen doping contents and sites can be facily controlled by tuning the doping temperature and mass ratio of ceria/urea. With the decrease of heat treatment temperature from 600 °C to 400 °C and the increase of ceria/urea mass ratio from 1:1 to 4:1, nitrogen preferred to be doped at interstitial sites. The completely different chemical environment of N_s and N_i may also bring out significant influence on the catalytic performance of CeO_2 like that in N-doped TiO_2 and N-doped MnO_2 .

Fig. 3b showed the O1s XPS spectra of the ceria catalysts. Three peaks are located at around 528.6 eV, 531.1 eV and 532.7 eV, assigned to the lattice oxygen (O_L), O atoms in the vicinity of OV (O_V), and the oxygen atoms on surface-adsorbed water (O_A), respectively [67]. The concentration of surface oxygen vacancies can be evaluated by the ratio of $[O_V]/[O_{total}]$ ($[O_L] + [O_V] + [O_A]$) according to the deconvoluted peak area of the O1s peak. The results were listed in Table 1. The ratio of $[O_V]/[O_{total}]$ obeys the sequence of NCe2-400 (24.5%) > NCe1-400 (23.1%) > NCe2-500 (22.6%) > NCe2-600 (22.0%) > NCe4-400 (20.6%) > CeO_2 (19.8%). All the N-doped CeO_2 samples have higher oxygen vacancies concentration than the pristine CeO_2 , and NCe2-400 has the highest one. This result suggests that N doping possibly facilitates the formation of OVs, and compared to N_s , N_i is more conducive to generating OVs. The surface OVs could also be verified by XPS spectra of Ce3d in Fig. 3c. To maintain the charge balance, the generation of OVs is

usually accompanied by the reduction of Ce^{4+} to Ce^{3+} . When one oxygen vacancy is formed in CeO_2 , two excess electrons are produced, which will reduce two Ce^{4+} cations to Ce^{3+} ions. The relative content of Ce^{3+} can be quantified by the percentage of the sum of the peak areas of Ce^{3+} (v_0 , v' , u_0 , and u') to that of the total peaks. The ratio of $[Ce^{3+}]/([Ce^{3+}] + [Ce^{4+}])$ also obeys the sequence of NCe2-400 (30.1%) > NCe1-400 (26.1%) > NCe2-500 (26.0%) > NCe2-600 (24.1%) > NCe4-400 (23.9%) > CeO_2 (18.8%). This result is consistent with the sequence of oxygen vacancy concentration obtained by O1s spectra. Those electron-rich defects of doped N, OVs, as well as Ce^{3+} in N-doped ceria might favor the activation of ozone and generate more reactive oxygen species (e.g., $\bullet OH$, surface O and $\bullet O_2^-$) due to the electrophilic character of ozone.

Fig. 4a presented the Raman spectra of CeO_2 , NCe2-400, NCe2-600. The band at 460 cm^{-1} attributes to the Raman mode of F_2g symmetry in cubic fluorite structure, and another two weak bands at 598 cm^{-1} and 836 cm^{-1} are attributed to oxygen vacancies (OVs) and η^2 peroxide species ($\eta^2-O_2^{2-}$) [30,31], respectively. Hence, the relative concentration of OVs and peroxide species in these three samples were quantified by the A_{598}/A_{460} and A_{836}/A_{460} ratio of integrated peak areas, respectively, and the results are listed in Table S1. The A_{598}/A_{460} ratio is 0.0224, 0.0412, and 0.0340 corresponding to CeO_2 , NCe2-400, NCe2-600. Among them, NCe2-400 has the highest concentration of OVs, followed by NCe2-600 and pure CeO_2 . It demonstrates that NCe2-400 has much more OVs than the other two samples, which is in accord with the results obtained from the XPS spectra. Moreover, NCe2-400 also has the highest concentration of peroxide species ($A_{836}/A_{460} = 0.0186$). It indicates that the absorbed O_2 on NCe2-400 is relatively easy to capture two electrons from NCe2-400.

Electron spin resonance (ESR) is another direct method to survey OVs and Ce^{3+} of the samples, and the outcomes are shown in Fig. 4b. Apparently, there are two obvious peaks at $g = 2.003$ and $g = 1.965$, which are attributed to quasi-electrons trapped in oxygen vacancies and Ce^{3+} , respectively [40]. ESR signal intensity of N-doped CeO_2 is stronger than that of the pristine CeO_2 and follows the order of NCe2-400 > NCe2-600 > CeO_2 . As the amount of doped-N changes, the ESR peak intensity of the sample follows the sequence of NCe2-400 > NCe1-400 > NCe4-400 > CeO_2 (Fig. S2). This trend also

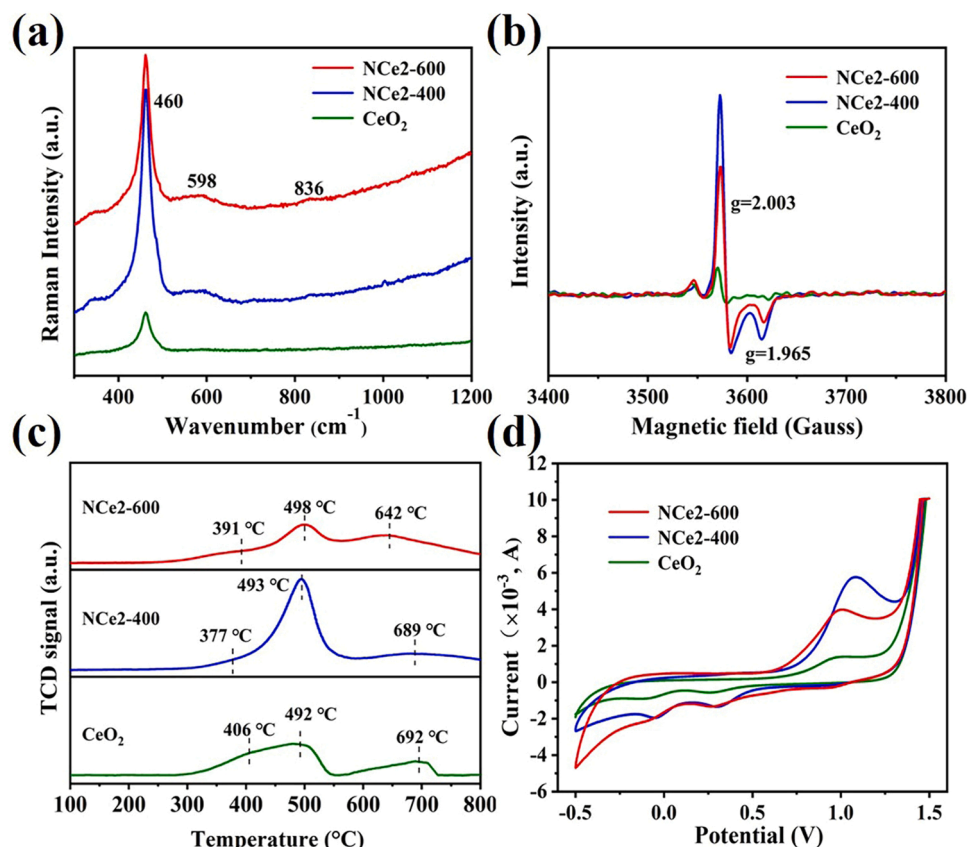


Fig. 4. (a) Raman spectra with excitation laser at 514 nm, (b) ESR patterns (c) H_2 -TPR and (d) CV curves of CeO_2 , N-Ce2-400 and N-Ce2-600 .

demonstrates that the introduction of N, especially N_i , is beneficial to the generation of OV. This observation is in consistent with the XPS spectra and Raman results, which will be furthermore investigated in the following DFT theoretical calculations.

The reducibility of CeO_2 in catalytic ozonation is the decisive step to realize the redox cycle since the oxidation step (i.e., from Ce^{3+} to Ce^{4+}) is relatively facile in the oxidation environment. Fig. 4c shows the H_2 -TPR profiles of CeO_2 , N-Ce2-400 and N-Ce2-600 . Peaks at low temperature (< 500 $^{\circ}\text{C}$) are attributed to the reduction of surface ceria, while peak at a high temperature (> 500 $^{\circ}\text{C}$) belongs to the reduction of bulk ceria. The first reduction temperature of CeO_2 , N-Ce2-400 and N-Ce2-600 centered at 406 $^{\circ}\text{C}$, 377 $^{\circ}\text{C}$, and 391 $^{\circ}\text{C}$, respectively. This indicates N-Ce2-400 is the most easily reduced, which will favor the redox cycle of the catalyst in the oxidation process. As shown in Table S2, the normalized H_2 consumption below 500 $^{\circ}\text{C}$ follows the order of N-Ce2-400 (0.835 $\text{mmol/g}_{\text{cat}}$) $>$ N-Ce2-600 (0.528 $\text{mmol/g}_{\text{cat}}$) $>$ CeO_2 (0.460 $\text{mmol/g}_{\text{cat}}$). Obviously, N doping also increases the content of reducible species, which agrees well with the XPS result that N doping can enhance the content of adsorbed oxygen on the surface [47]. It can be observed that N-Ce2-400 , i.e., N_i -doped ceria, has the lowest reduction temperature and the highest H_2 consumption. Compared with the N_s doping, N_i doping greatly enhances the reducibility and mobility of surface oxygen species on the ceria.

To further disclose the redox ability of pure CeO_2 and N-doped CeO_2 , the CV (cyclic voltammetry) curves were executed. As shown in Fig. 4d, the anodic current oxidation peak is attributed to the oxidation of Ce^{3+} to Ce^{4+} , and the cathodic one corresponds to the reduction of Ce^{4+} to Ce^{3+} . Apparently, the current densities of both reduction and oxidation curves for N-Ce2-400 are much higher than those of CeO_2 and N-Ce2-600 , indicating that more electrons are transferred and participated in the redox reaction over N-Ce2-400 [68]. Therefore, N-Ce2-400 has the greatest ability to conduct a redox cycle, which is conducive to

catalytic ozonation.

3.3. Catalytic performance of N_i - and N_s -doped ceria

From the above discussion, N_i - and N_s -doping greatly affected the defects and redox properties of ceria, which will finally impose significant influence on their catalytic activity. Herein the catalytic activity of various N-doped ceria was investigated by the removal of both SMZ and their TOC. As shown in Fig. 5a and b, the extent of SMZ removal within 30 min by adsorption could be ignored, and in the single ozonation process, it was $55.4 \pm 2.5\%$. With the introduction of pure ceria into the ozonation, SMZ was degraded by $64.5 \pm 2.5\%$, whereas all the N-doped ceria furthermore strengthened the SMZ removal. Among them, N-Ce2-400 with 100% N_i and the richest OV. exhibited the best catalytic activity. With it, the elimination of SMZ within 30 min reached as high as $93.7 \pm 1.9\%$, about 38.3% higher than that of single ozonation. For N-Ce2-600 with 50.1% N_s , the degradation of SMZ in 30 min was only $71.9 \pm 2.0\%$, about 21.8% lower than that of N-Ce2-400 . The enhancement on the degradation of SMZ by catalytic ozonation follows the order of $\text{N-Ce2-400} > \text{N-Ce2-500} > \text{N-Ce2-600}$ and $\text{N-Ce2-400} > \text{N-Ce1-400} > \text{N-Ce4-400}$, respectively. It is almost in accordance with the order of N_i percentage and OV content in each sample. It is noted that the catalytic activity of N-Ce2-500 , which has similar N_{total} content to N-Ce2-400 , is between that of N-Ce2-400 and N-Ce2-600 . In addition, N-Ce1-400 obtained the highest N_{total} content among all the N-doped ceria whereas it showed worse catalytic activity than N-Ce2-400 . These results furthermore demonstrated the location of doped nitrogen has great influence on the catalytic ozonation. Fig. 5b and d showed that the abatement of SMZ over catalysts can be well fitted by the pseudo first-order kinetics with the relatively high values of R^2 (> 0.95). Regarded N-Ce2-400 , the first-order rate constant (k_1) is $8.77 \times 10^{-2} \text{ min}^{-1}$, 4.1, 3.3 and 2.1 times that of single ozonation, pure

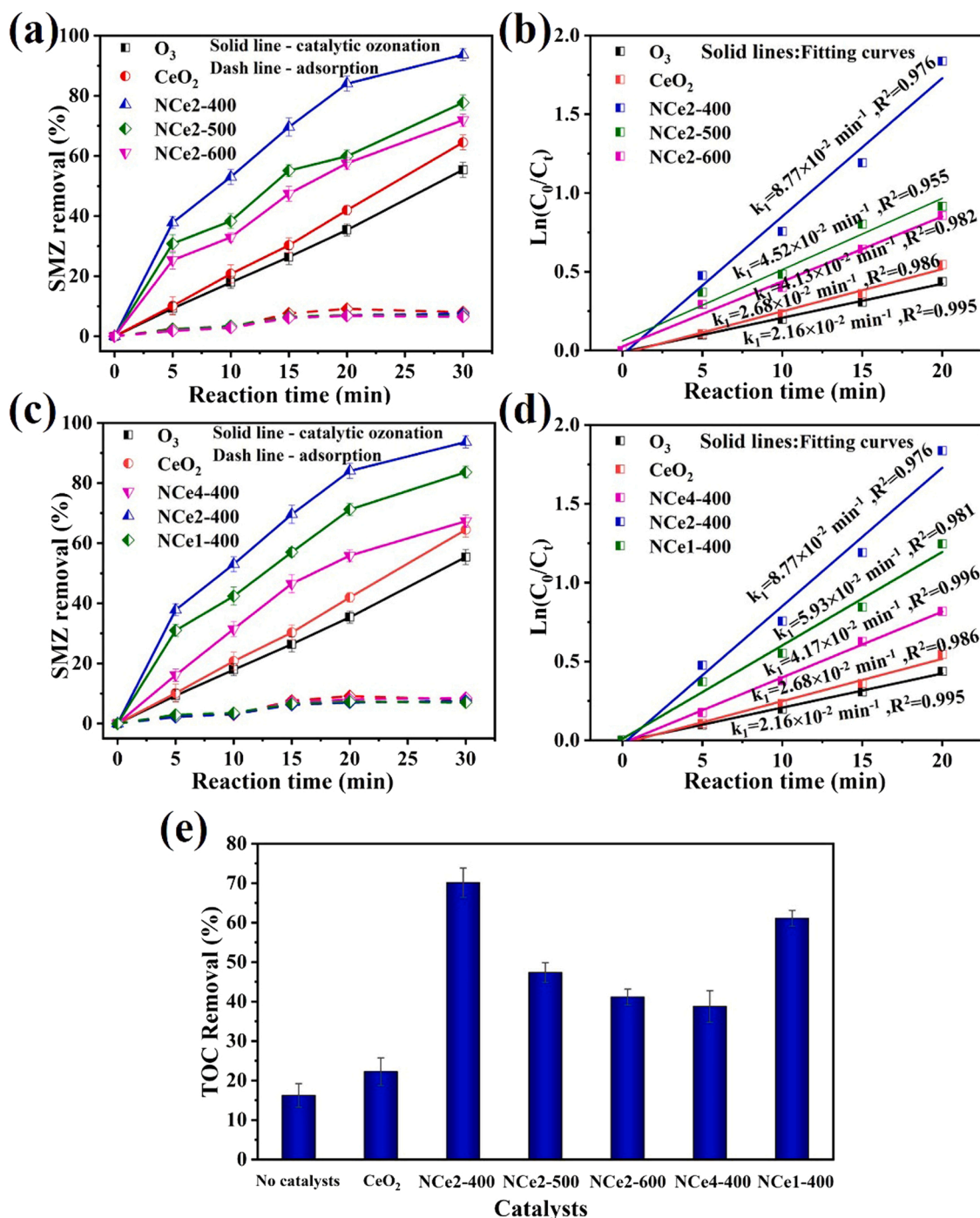


Fig. 5. SMZ removal and pseudo first-order kinetics fitting for SMZ removal in catalytic ozonation with ceria treated at various N-doping temperature (a, b) and with ceria treated at various ceria/urea mass ratio (c, d); (e) TOC removal within the reaction time of 90 min over various catalysts.

CeO_2 and N-Ce2-600, respectively.

To further observe the catalytic abilities of catalysts, the TOC removal within 90 min was presented in Fig. 5e. Single ozonation has a very low TOC removal of $16.2 \pm 3.0\%$, indicating that SMZ and most of the degradation intermediates from SMZ are resistant to ozone. With the introduction of N-doped ceria into the oxidation system, TOC removal has been greatly promoted. In particular, TOC removal is up to $70.0 \pm 2.5\%$ with the catalyst of N-Ce2-400, implying that most SMZ is completely mineralized into CO_2 and H_2O . Meanwhile, the order of TOC removal is consistent with that of SMZ degradation with different catalysts.

There are several reasons for the excellent catalytic performance of

N-Ce2-400. Firstly, N-Ce2-400 has more electron-rich defects of N_i , OV and Ce^{3+} as indicated by XPS, Raman and ESR results. With the introduction of N atom, the long-term periodic order of lattice O was destroyed, and the OV and Ce^{3+} were produced to rebalance the charge [69]. Compared to N_s , N_i is directly connected to the O atom in the CeO_2 lattice, which has the stronger interaction with nearby O atoms. Therefore, the N_i makes oxygen species more active and produces more defects in CeO_2 . As discussed above, these electron-rich defects favor the adsorption and activation of electron-deficient ozone. As shown in Table S1, N-Ce2-400 has the highest concentration of peroxide species ($\eta^2-O_2^{2-}$). It indicates that the adsorbed oxygen on the surface N-Ce2-400 can most easily capture two electrons from the ceria. Since O_3 is

much more electron-deficient than oxygen, it is expected that O_3 can be more readily activated by capturing electrons from N-Ce2-400 than the other ceria. In addition, N-Ce2-400 also exhibits the best redox ability as verified by H_2 -TPR and CV, which favor the catalytic process. In summary, the abundance of N_i , OV, Ce^{3+} and facile redox property make N-Ce2-400 exhibit excellently in the catalytic oxidation of SMZ by ozone.

3.4. Exploration of catalytic mechanism over N_i - and N_s -doped ceria

3.4.1. Experimental investigation

Generally, the catalytic performance is improved because the catalysts promote the decomposition of ozone to produce more reactive oxygen species (ROS) in the catalytic ozonation process, such as surface oxygen atom (O^*), $\bullet OH$, $\bullet O_2^-$ and 1O_2 . These ROS play important roles in pollutant degradation and final mineralization. To demonstrate it clearly, the ozone decomposition over various ceria catalysts was initially investigated. As shown in Fig. 6a, ozone degraded rapidly within the first 10 min in all cases. The addition of ceria catalysts fastened the decomposition rate in the whole period. Among all the ceria, N-Ce2-400 performed the best, followed by N-Ce2-600 and the worst was CeO_2 . It indicates that N-Ce2-400 favor to the adsorption and decomposition of ozone. However, the pollutant degradation also depends greatly on the active species derived from the decomposition of ozone. To reveal the active species involved in the reaction by N-Ce2-400, ROS quenching experiments and ESR techniques were conducted.

To identify the formation of $\bullet OH$, $\bullet O_2^-$ and 1O_2 , three scavengers, i.e., tert-butanol (TBA, $\bullet OH$ scavenger), 1,4-benzoquinone (p-BQ, $\bullet O_2^-$ scavenger), and sodium azide (NaN_3 , 1O_2 scavenger) were added into the SMZ-containing oxidation system, respectively. As shown in Fig. 6b, the SMZ degradation was obviously inhibited by all three scavengers. Among them, TBA reduced the removal of SMZ from 93.7% to 29.1%, which was reduced to 59.8% and 72.3% by adding p-BQ and NaN_3 , respectively. In the existence of TBA, p-BQ and NaN_3 , the first-order rate constant (k_1) was reduced to 0.18, 0.39 and 0.55 times that without the addition of any quenching agent (Fig. 6c). It indicates that $\bullet OH$ radicals were the main active species in the catalytic ozonation, $\bullet O_2^-$ radicals showed moderate contribution and 1O_2 played the least role. As is known, the oxidation potential of $\bullet O_2^-$ (1.35 V) is much lower than that of $\bullet OH$ (2.80 V) and 1O_2 (2.20 V) at neutral pH [70]. Obviously, $\bullet O_2^-$ radicals with such a low oxidation potential may not directly oxidize the pollutants like $\bullet OH$ and 1O_2 radicals. However, $\bullet O_2^-$ radicals are the important intermediates that produce many other stronger radicals in chain reactions. The quenching of $\bullet O_2^-$ by p-BQ possibly decreased the formation of these stronger radicals and thereof inhibited the degradation of SMZ.

The existence of $\bullet OH$, $\bullet O_2^-$ and 1O_2 within a reaction time of 20 min in single ozonation and ceria-mediated catalytic ozonation were further identified by ESR techniques. The results are compared in terms of the relative intensity of ESR signals in Fig. 7a-c. With the addition of DMPO trapping agent, a characteristic “1:2:2:1” pattern of DMPO- $\bullet OH$ was observed in all four cases (Fig. 7a). Fig. 7b showed an ESR “1:1:1:1” pattern characteristic of DMPO/DMSO- $\bullet O_2^-$ with the addition of DMPO/DMSO trapping agent. A characteristic “1:1:1” pattern of TEMP- 1O_2 adduct with the addition of TEMP trapping agent was presented in Fig. 7c. The intensity of the signals of all three ROS ($\bullet OH$, $\bullet O_2^-$ and 1O_2) followed the order of N-Ce2-400 > N-Ce2-600 > CeO_2 > single ozonation. In other words, N-doped CeO_2 , especially N-Ce2-400, presented stronger ESR signals of each ROS compared to CeO_2 and single ozonation. This result confirms again that N doping, especially N_i doping in the modification of ceria, promotes the decomposition of ozone to produce more ROS.

3.4.2. DFT calculation

Catalytic ozonation is closely related to the adsorption and decomposition of ozone on the surface of a catalyst. Density functional theory

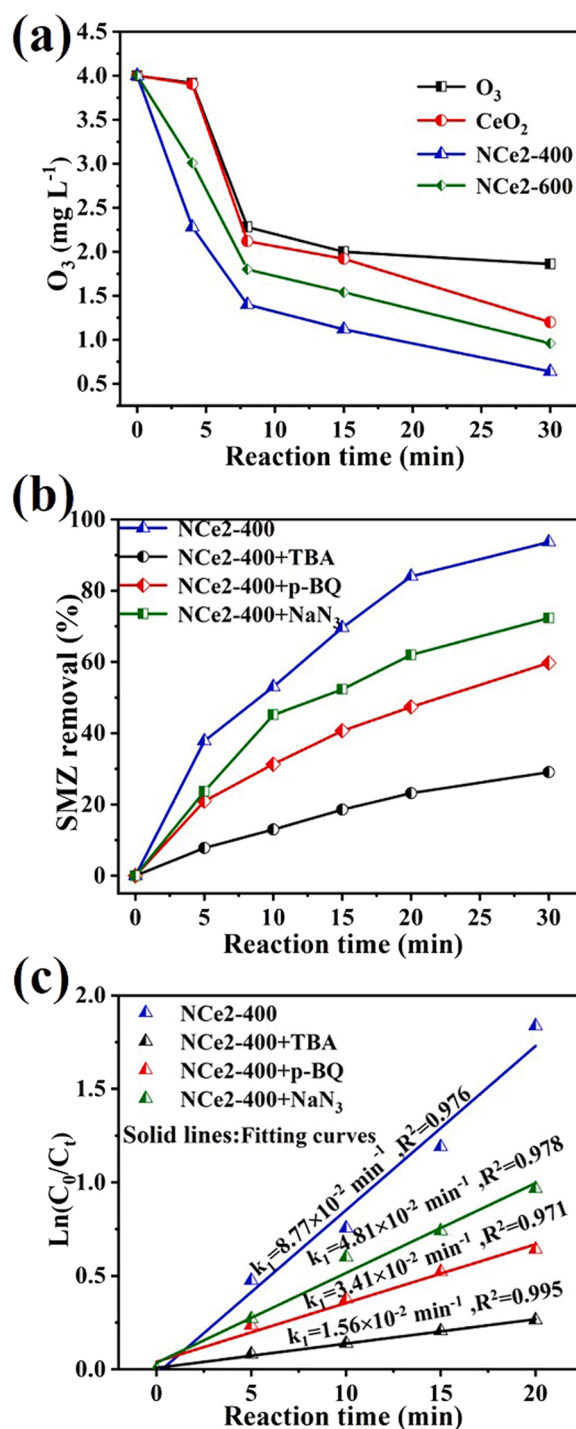


Fig. 6. (a) Evolution of ozone concentration over time in ozonation and catalytic ozonation, (b) SMZ removal and (c) pseudo first-order kinetics fitting in N-Ce2-400 mediated catalytic ozonation with 1 mM of different scavengers.

(DFT) calculations were performed to understand the enhanced mechanism of N-doped ceria, including the effects of N_i and N_s on the formation energy of OV, the atomic and electronic structure of CeO_2 , as well as the adsorption and decomposition of ozone on N-doped ceria at the atomic level.

It has been widely reported that OV is the active sites for the adsorption and activation of ozone. As discussed above, it is found that nitrogen doping at both interstitial and substitutional sites can lead to the formation of OV. Therefore, a DFT calculation was carried out to investigate the formation energy of OV in the presence of N_s or N_i . Since

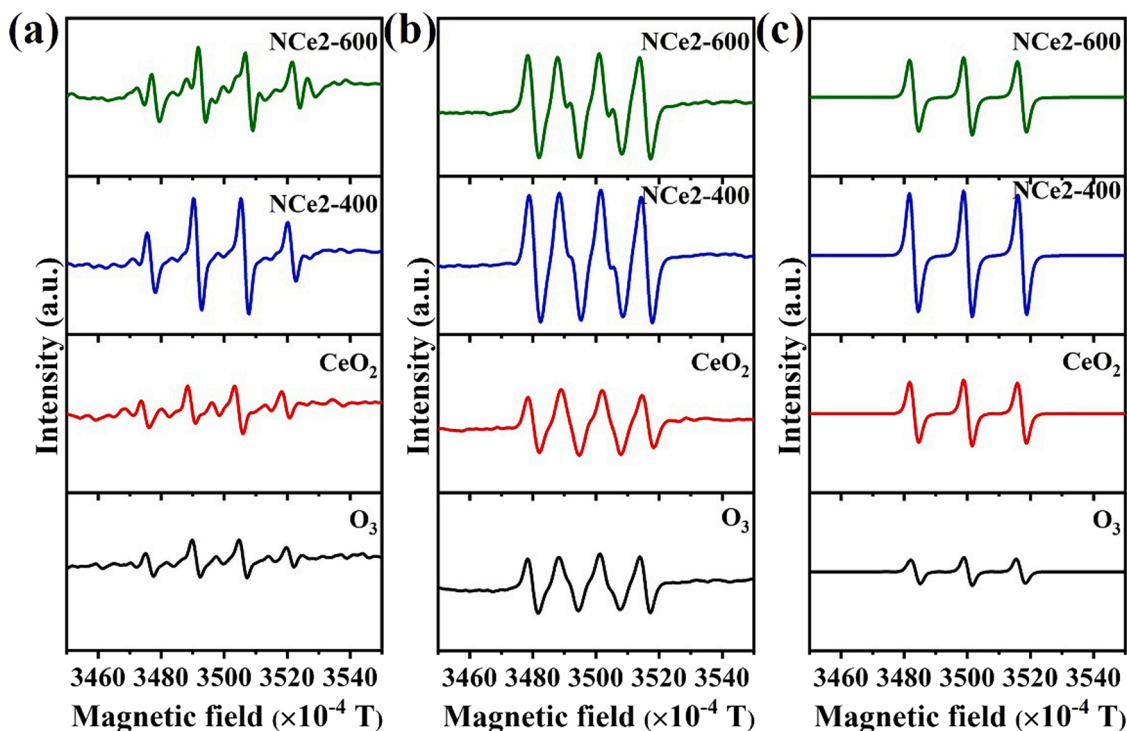


Fig. 7. ESR spectra of (a) DMPO•OH, (b) DMPO/DMSO•O₂ and (c) TEMP•¹O₂ adducts in single ozonation and catalytic ozonation with the catalyst of CeO₂, NCe2-400 and NCe2-600.

the most exposed crystal facet in all ceria catalysts was (110) (Fig. 2), we built and optimized three slabs with the perfect (110) plane of CeO₂ (labeled as CeO₂), (110) plane with N_i (labeled as N_i-CeO₂) and (110) plane with N_s (labeled as N_s-CeO₂).

The formation energy of OV_s (ΔE_{OV}) in CeO₂, N_i-CeO₂, and N_s-CeO₂ were calculated to be 2.71 eV, 0.87 eV and 2.41 eV, respectively (Fig. 8). The low ΔE_{OV} indicates the easy formation of OV_s. Herein two conclusions can be drawn, (1) nitrogen doping, regardless of the doping sites, reduced the ΔE_{OV} . It suggests that N doping can activate O atoms near the N atom and thus favor the formation of OV_s; (2) compared to the N_s-CeO₂ ($\Delta E_{OV} = 2.41$ eV), the formation energy of OV_s in N_i-CeO₂ ($\Delta E_{OV} = 0.87$ eV) decreased remarkably. It indicates that N_i doping is more conducive to the formation of OV_s than N_s doping. As discussed above, N_s replaces the oxygen atom to form the Ce-N-Ce-O bond, but N_i is directly inserted into the Ce-O bond to form the Ce-N-O bond. Obviously, the interaction between N_i and the nearby oxygen in Ce-N-O is much stronger than that in Ce-N-Ce-O, which enhance the activity of oxygen. The much lower ΔE_{OV} of N_i-CeO₂ also explained the presence of the most OV_s in NCe2-400 as demonstrated by Raman, XPS, and ESR results, which has 100% N_i in the lattice.

To reveal the effect of the coexistence of doped N and the resulting oxygen vacancy in the catalytic process, the adsorption and dissociation of ozone over the above optimized N_i-CeO₂ and N_s-CeO₂ with an oxygen vacancy in each structure was furthermore investigated and compared by DFT calculations. According to the literatures, the adsorbed ozone usually tended to be dissociated into surface oxygen atom (O*) or/and superoxide radical (•O₂⁻), which then initiate a series of radical chain reactions [30,31]. Herein the generation of the surface oxygen atom is investigated in ozone decomposition mechanism as one of the initiation steps. Fig. 9 shows the optimized atomic and electronic structures and the calculated potential energy profiles for the one-step reaction between an ozone molecule and the Ce atom around the oxygen vacancy and nitrogen of N_i-CeO₂, and N_s-CeO₂, respectively. After the geometry optimization of the physisorption (IS, initial state) and the chemisorption (FS, final state) of ozone on N_i-CeO₂ and N_s-CeO₂, as well as the transition state (TS) search, a reaction path from IS to FS was created in

Fig. 9a. The bond length (indicated by blue numbers) and the losses and gains of atom charge calculated from the Bader electrons (indicated by black numbers) were displayed in Figs. 9b and S3. As shown in Figs. 9a, b & S3, for IS in both cases, the ozone relaxed near the Ce around the oxygen vacancy and nitrogen. The adsorption energy of ozone on N_i-CeO₂ and N_s-CeO₂ were -2.40 eV and -2.03 eV, respectively. It indicates that the adsorption of ozone over both N-doped CeO₂ stabilizes their structures. That is to say, the coexistence of doped nitrogen and oxygen vacancy, especially the N_i and then N_s, favor the adsorption of ozone. Meanwhile, the bond between O1 in ozone with the Ce in both slabs is initially set at about 2.85 Å, and that of O1-O2 and O2-O3 in the optimized ozone molecule is 1.29 Å (Fig. S3). After the relaxation, the Ce-O1 band in N_i-CeO₂ and N_s-CeO₂ decreased to 2.53 Å and 2.25 Å while O1-O2 band increased to 1.36 Å and 1.49 Å, respectively. The O1 in the IS of N_i-CeO₂ and N_s-CeO₂ decreased from about zero to -0.44|e| and -0.50 |e|, respectively. Obviously, O1 gained electrons from N_i-CeO₂ more or less depending on the location of nitrogen. Moreover, the total charge of O2-O3 in N_i-CeO₂ is close to zero. Combined with the change in bond length, it shows that ozone tends to dissociate into a surface atom oxygen (O*) and an oxygen molecule. In contrast, the total charge of O2-O3 in N_s-CeO₂ is -0.41|e|, implying that ozone tends to dissociate into a surface atom oxygen (O*) and an O₂⁻. Therefore, such structure was set as the FS. Based on the energy of IS and FS, the dissociation of ozone was found to be slightly exothermic in the case of N_i-CeO₂ while slightly endothermic in N_s-CeO₂, and the barrier energy in this step for N_i-CeO₂ and N_s-CeO₂ were 0.32 eV and 0.50 eV (Fig. 9a), respectively. Herein the barrier energy for the activation of ozone over N_i-CeO₂ is much lower than that of N_s-CeO₂, which partly explains the higher catalytic activity of N_i-CeO₂. It demonstrates that the introduction of nitrogen to the interstitial site (N_i) of CeO₂ is also more conducive to the activation of ozone than that to the substitutional site (N_s). As reported, the surface-adsorbed oxygen atom has high oxidation potential (2.43 V), which would either oxidize the pollutants or react with another O₃ molecule to form •OH radicals [71]. The above experimental and theory calculation results prove that N-doping can reduce oxygen formation energy and enhance both the adsorption and dissociation of

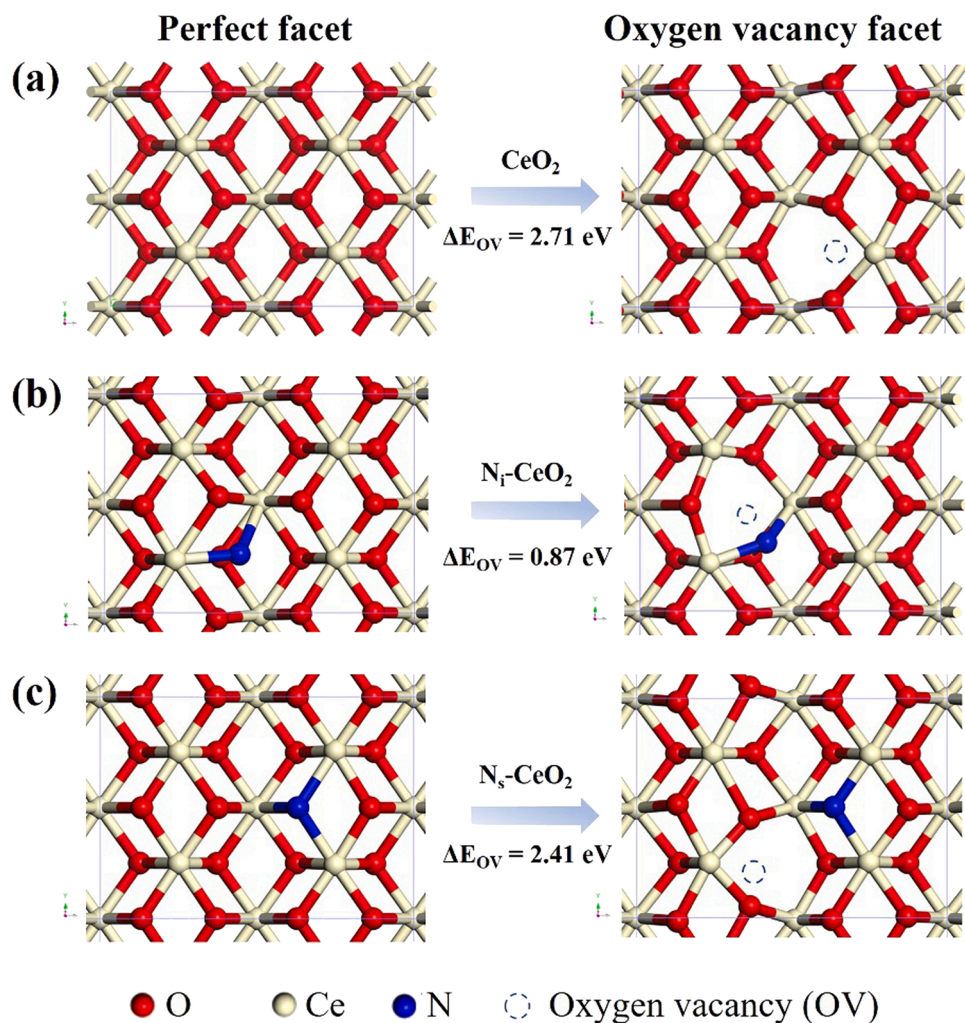


Fig. 8. Formation energy of an oxygen vacancy over (a) CeO_2 , (b) Ni-CeO_2 and (c) $\text{N}_5\text{-CeO}_2$.

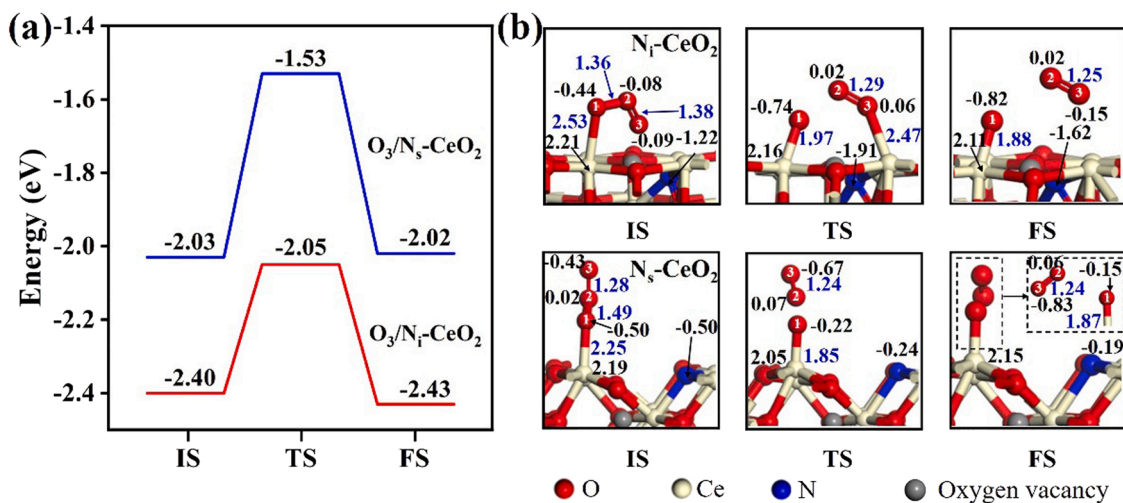


Fig. 9. Results of DFT calculations. (a) energy paths for the activation of ozone on Ni , N_5 -doped CeO_2 . (b) atomic and electronic structure of ozone adsorbed on Ni-CeO_2 and $\text{N}_5\text{-CeO}_2$ (Red spheres are oxygen, blue spheres are nitrogen, white spheres are cerium and gray spheres are oxygen vacancies).

ozone into ROS. Compared with N_5 , Ni performed even more excellently, thus better improved the catalytic performance of Ni -doped CeO_2 .

4. Conclusion

The identification of N-doping sites and the tuning of doping sites in N-doped ceria were performed for the first time. The N atoms can be

doped into interstitial sites or substitutional sites in CeO₂ lattice by facilely adjusting heat treatment temperature and urea amount in a facile urea-assisted heat treatment method. N atoms are preferentially inserted into the interstitial sites at lower temperature and higher ceria/urea mass ratio. When the temperature or urea amount increases, N atoms can be also sat at the substitutional sites (N_s) or transformed to the interstitial sites (N_i). Both experiments and DFT calculations demonstrate that compared to N_s, N_i strengthened the formation of oxygen vacancies (OVs), the adsorption of ozone and their dissociation into reactive oxygen species (e.g., •OH, •O₂⁻, surface *O), which boosted the oxidation of pollutants in catalytic ozonation.

CRedit authorship contribution statement

Shujuan Zhan: Methodology, Software, Validation, Investigation, Writing. **Huating Huang:** Investigation, Data curation. **Chun He:** Conceptualization, Writing – review & editing. **Ya Xiong:** Conceptualization, Writing – review & editing, Funding acquisition. **Ping Li:** Supervision, Conceptualization, Writing – review & editing. **Shuanghong Tian:** Project administration, Supervision, Conceptualization, Writing – review & editing, Methodology, Funding acquisition.

Declaration of Competing Interest

The authors declare that they have no known competing financial interests or personal relationships that could have appeared to influence the work reported in this paper.

Data availability

Data will be made available on request.

Acknowledgments

The research is supported by the National Natural Science Foundation of China (21777196, 21976215), Guangdong Basic and Applied Basic Research Foundation (2020A1515011324), and Guangzhou Municipal Science and Technology Project (202002030417).

Appendix A. Supplementary material

N₂ adsorption-desorption isotherms of CeO₂, N/Ce2-400 and N/Ce2-600, ESR patterns of CeO₂, N/Ce4-400, N/Ce2-400 and N/Ce1-400, Geometry structures before and after optimization of ozone adsorption on N_i-CeO₂, and N_s-CeO₂, Raman and H₂-TPR results of CeO₂, N/Ce2-400 and N/Ce2-600.

Supplementary data associated with this article can be found in the online version at doi:10.1016/j.apcatb.2022.122040.

References

- [1] T. Boeckel, S. Gandra, A. Ashok, Global antibiotic consumption 2000 to 2010: an analysis of national pharmaceutical sales data, *Lancet Infect. Dis.* 14 (2014) 742–750.
- [2] Q. Zhang, G. Ying, C. Pan, Y. Liu, J. Zhao, Comprehensive evaluation of antibiotics emission and fate in the river basins of China: source analysis, multimedia modeling, and linkage to bacterial resistance, *Environ. Sci. Technol.* 49 (2015) 6772–6782.
- [3] A. Wang, Z. Hua, C. Chen, W. Wei, B. Huang, S. Hou, X. Li, J. Fang, Radical chemistry and PPCP degradation in the UV/peroxydisulfate process in the presence of chloride at freshwater levels, *Chem. Eng. J.* 426 (2021), 131276.
- [4] M. Huber, S. Canonica, G. Park, U. Gunten, Oxidation of pharmaceuticals during ozonation and advanced oxidation processes, *Environ. Sci. Technol.* 37 (2003) 1016–1024.
- [5] R. Andreozzi, V. Caprio, A. Insola, R. Marotta, Advanced oxidation processes (AOP) for water purification and recovery, *Catal. Today* 53 (1999) 51–59.
- [6] X. Duan, H. Sun, Y. Wang, J. Kang, S. Wang, N-doping-induced nonradical reaction on single-walled carbon nanotubes for catalytic phenol oxidation, *ACS Catal.* 5 (2015) 553–559.
- [7] J. Wang, H. Chen, Catalytic ozonation for water and wastewater treatment: recent advances and perspective, *Sci. Total Environ.* 704 (2020), 135249.
- [8] J. Chen, S. Tian, J. Lu, Y. Xiong, Catalytic performance of MgO with different exposed crystal facets towards the ozonation of 4-chlorophenol, *Appl. Catal. A Gen.* 506 (2015) 118–125.
- [9] Q. Dai, Z. Zhang, T. Zhan, Z. Hu, J. Chen, Catalytic ozonation for the degradation of 5-sulfosalicylic acid with spinel-type ZnAl₂O₄ prepared by hydrothermal, sol-gel, and coprecipitation methods: a comparison study, *ACS Omega* 3 (2018) 6506–6512.
- [10] A. Ziyilan-Yavas, N. Ince, Catalytic ozonation of ibuprofen with ultrasound and Fe-based catalysts, *Catal. Today* 240 (2015) 2–8.
- [11] J. Wang, Y. Lou, C. Xu, S. Song, W. Liu, Magnetic lanthanide oxide catalysts: an application and comparison in the heterogeneous catalytic ozonation of diethyl phthalate in aqueous solution, *Sep. Purif. Technol.* 159 (2016) 57–67.
- [12] J. Vittenet, W. Aboussaoud, J. Mendret, J.-S. Pic, H. Debellfontaine, N. Lesage, K. Faucher, M.-H. Manero, F. Thibault-Starzyk, H. Leclerc, A. Galarneau, S. Brosillon, Catalytic ozonation with γ-Al₂O₃ to enhance the degradation of refractory organics in water, *Appl. Catal. A Gen.* 504 (2015) 519–532.
- [13] B. Wang, H. Zhang, F. Wang, X. Xiong, K. Tian, Y. Sun, T. Yu, Application of heterogeneous catalytic ozonation for refractory organics in wastewater, *Catalysts* 9 (2019).
- [14] Y. Tong, L. Song, S. Ning, S. Ouyang, J. Ye, Photocatalysis-enhanced photothermocatalysis of water-gas shift reaction under H₂-rich and low-temperature condition over CeO₂/Cu_{1.5}Mn_{1.5}O₄ catalyst, *Appl. Catal. B Environ.* 298 (2021), 120551.
- [15] W. Yu, W. Wang, C. Ma, S. Li, K. Wu, J. Zhu, H. Zhao, C. Yan, C. Jia, Very high loading oxidized copper supported on ceria to catalyze the water-gas shift reaction, *J. Catal.* 402 (2021) 83–93.
- [16] Z. Zhao, M. Wang, P. Ma, Y. Zheng, J. Chen, H. Li, X. Zhang, K. Zheng, Q. Kuang, Z. Xie, Atomically dispersed Pt/CeO₂ catalyst with superior CO selectivity in reverse water gas shift reaction, *Appl. Catal. B Environ.* 291 (2021), 120101.
- [17] Y. Lee, H. Kim, C. Jeong, D. Jeong, Effects of precipitants on the catalytic performance of Cu/CeO₂ catalysts for the water-gas shift reaction, *Catal. Sci. Technol.* 11 (2021) 6380–6389.
- [18] T. Fiuzza, I. D. Onsalves, D. Gomes, Zanchet, CeO₂-supported Au and AuCu catalysts for CO oxidation: Impact of activation protocol and residual chlorine on the active sites, *Catal. Today* 381 (2021) 171–180.
- [19] Y. Wang, J. Ma, X. Wang, Z. Zhang, J. Zhao, J. Yan, Y. Du, H. Zhang, D. Ma, Complete CO oxidation by O₂ and H₂O over Pt-CeO_{2-x}/MgO following Langmuir-Hinshelwood and Mars-van Krevelen mechanisms, respectively, *ACS Catal.* 11 (2021) 11820–11830.
- [20] A. Cruz, E. Assaf, J. Gomes, J. Assaf, Active copper species of co-precipitated copper-ceria catalysts in the CO-PROX reaction: an in situ XANES and DRIFTS study, *Catal. Today* 381 (2021) 42–49.
- [21] W. Wang, Y. Liu, L. Wang, W. Zhan, Y. Guo, Y. Guo, Soot combustion over Ag catalysts supported on shape-controlled CeO₂, *Catal. Today* 376 (2021) 9–18.
- [22] V. Alcalde-Santiago, E. Bailon-Garcia, A. Davo-Quinero, D. Lozano-Castello, A. Bueno-Lopez, Three-dimensionally ordered macroporous PrO_x: an improved alternative to ceria catalysts for soot combustion, *Appl. Catal. B Environ.* 248 (2019) 567–572.
- [23] R. Ashikaga, K. Murata, T. Ito, Y. Yamamoto, S. Arai, A. Satsuma, Tuning the oxygen release properties of CeO₂-based catalysts by metal-support interactions for improved gasoline soot combustion, *Catal. Sci. Technol.* 10 (2020) 7177–7185.
- [24] A. Hernandez-Gimenez, L. Xavier, A. Bueno-Lopez, Improving ceria-zirconia soot combustion catalysts by neodymium doping, *Appl. Catal. A Gen.* 462 (2013) 100–106.
- [25] H. Chang, X. Chen, J. Li, L. Ma, C. Wang, C. Liu, J. Schwank, J. Hao, Improvement of activity and SO₂ tolerance of Sn-modified MnO_x-CeO₂ catalysts for NH₃-SCR at low temperatures, *Environ. Sci. Technol.* 47 (2013) 5294–5301.
- [26] L. France, Q. Yang, W. Li, Z. Chen, J. Guang, D. Guo, L. Wang, X. Li, Ceria modified FeMnO_x-enhanced performance and sulphur resistance for low-temperature SCR of NO_x, *Appl. Catal. B Environ.* 206 (2017) 203–215.
- [27] H. Liu, Z. Fan, C. Sun, S. Yu, S. Feng, W. Chen, D. Chen, C. Tang, F. Gao, L. Dong, Improved activity and significant SO₂ tolerance of samarium modified CeO₂-TiO₂ catalyst for NO selective catalytic reduction with NH₃, *Appl. Catal. B Environ.* 244 (2019) 671–683.
- [28] X. Wen, C. Niu, L. Zhang, C. Liang, G. Zeng, A novel Ag₂O/CeO₂ heterojunction photocatalysts for photocatalytic degradation of enrofloxacin: possible degradation pathways, mineralization activity and an in depth mechanism insight, *Appl. Catal. B Environ.* 221 (2018) 701–714.
- [29] M. Zeng, Y. Li, M. Mao, J. Bai, L. Ren, X. Zhao, Synergetic effect between photocatalysis on TiO₂ and thermocatalysis on CeO₂ for gas-phase oxidation of benzene on TiO₂/CeO₂ nanocomposites, *ACS Catal.* 5 (2015) 3278–3286.
- [30] X. Chen, H. Yang, C. Au, S. Tian, Y. Xiong, Y. Chang, Efficiency and mechanism of pollutant degradation and bromate inhibition by faceted CeO₂ catalyzed ozonation: experimental and theoretical study, *Chem. Eng. J.* 390 (2020), 124480.
- [31] X. Chen, S. Zhan, D. Chen, C. He, S. Tian, Y. Xiong, Grey Fe-CeO_{2-x} for boosting photocatalytic ozonation of refractory pollutants: roles of surface and bulk oxygen vacancies, *Appl. Catal. B Environ.* 286 (2021), 119928.
- [32] E. Ginting, E. Peterson, J. Zhou, Scanning tunneling microscopy studies of Mn-doped CeO_x(111) interfaces, *Appl. Catal. B Environ.* 197 (2016) 337–342.
- [33] T. Lei, H. Guo, C. Miao, W. Hua, Y. Yue, Z. Gao, Mn-doped CeO₂ nanorod supported Au catalysts for dehydrogenation of ethane with CO₂, *Catalysts* 9 (2019).
- [34] S. Li, S. Yan, Y. Xia, B. Cui, Y. Pu, Y. Ye, D. Wang, Y. Liu, B. Chen, Oxidative reactivity enhancement for soot combustion catalysts by co-doping silver and manganese in ceria, *Appl. Catal. A Gen.* 570 (2019) 299–307.

- [35] Y. Wang, C. Yin, H. Qin, Y. Wang, Y. Li, X. Li, Y. Zuo, S. Kang, L. Cui, A urea-assisted template method to synthesize mesoporous N-doped CeO₂ for CO₂ capture, *Dalton Trans.* 44 (2015) 18718–18722.
- [36] N. Zheng, T. Ouyang, Y. Chen, Z. Wang, D. Chen, Z. Liu, Ultrathin CdS shell-sensitized hollow S-doped CeO₂ spheres for efficient visible-light photocatalysis, *Catal. Sci. Technol.* 9 (2019) 1357–1364.
- [37] H. Miao, G. Huang, J. Liu, B. Zhou, A. Pan, W. Huang, G. Huang, Origin of enhanced photocatalytic activity of F-doped CeO₂ nanocubes, *Appl. Surf. Sci.* 370 (2016) 427–432.
- [38] L. Zhou, M. Cai, X. Zhang, N. Cui, G. Chen, G. Zou, In-situ nitrogen-doped black TiO₂ with enhanced visible-light-driven photocatalytic inactivation of *Microcystis aeruginosa* cells: synthesis, performance and mechanism, *Appl. Catal. B Environ.* 272 (2020), 119019.
- [39] Y. Hwang, S. Yang, H. Lee, Surface analysis of N-doped TiO₂ nanorods and their enhanced photocatalytic oxidation activity, *Appl. Catal. B Environ.* 204 (2017) 209–215.
- [40] Q. Cong, L. Chen, X. Wang, H. Ma, J. Zhao, S. Li, Y. Hou, W. Li, Promotional effect of nitrogen-doping on a ceria unary oxide catalyst with rich oxygen vacancies for selective catalytic reduction of NO with NH₃, *Chem. Eng. J.* 379 (2020), 122302.
- [41] D. Dao, H. Jung, T. Nguyen, S.-W. Ki, H. Son, K.-B. Bae, T. Le, Y.-H. Cho, J.-K. Yang, Y.-T. Yu, S. Back, I.-H. Lee, Defect-rich N-doped CeO₂ supported by N-doped graphene as a metal-free plasmonic hydrogen evolution photocatalyst, *J. Mater. Chem. A* 9 (2021) 10217–10230.
- [42] C. Liu, H. Sun, J. Qian, Z. Chen, Y. Lv, F. Chen, X. Lu, Z. Wu, Biotemplating synthesis and photocatalytic activities of N-doped CeO₂ microcapsule tailored by hemerocallis pollen, *Adv. Powder Technol.* 28 (2017) 2741–2746.
- [43] J. Iqbal, N. Shah, M. Sayed, J. Khan, N. Muhammad, Z. Khan, R. Saif ur, M. Naseem, F. Howari, Y. Nazzal, N. Niazi, A. Hussein, K. Polychronopoulou, Synthesis of nitrogen-doped Ceria nanoparticles in deep eutectic solvent for the degradation of sulfamethaxazole under solar irradiation and additional antibacterial activities, *Chem. Eng. J.* 394 (2020), 124869.
- [44] C. Wu, Solvothermal synthesis of N-doped CeO₂ microspheres with visible light-driven photocatalytic activity, *Mater. Lett.* 139 (2015) 382–384.
- [45] Y. Jia, H. Li, N. Hu, Q. Wang, Enhanced visible light adsorption of heavily nitrogen doped CeO₂ thin film via ion beam assisted deposition, *Rare Met. Mater. Eng.* 45 (2016) 1988–1991.
- [46] Y. Ma, X. Zhang, L. Cao, J. Lu, Effects of the morphology and heteroatom doping of CeO₂ support on the hydrogenation activity of Pt single-atoms, *Catal. Sci. Technol.* 11 (2021) 2844–2851.
- [47] T. He, X. Zeng, S. Rong, The controllable synthesis of substitutional and interstitial nitrogen-doped manganese dioxide: the effects of doping sites on enhancing the catalytic activity, *J. Mater. Chem. A* 8 (2020) 8383–8396.
- [48] G. Kresse, J. Furthmüller, Efficiency of ab-initio total energy calculations for metals and semiconductors using a plane-wave basis set, *Comput. Mater. Sci.* 6 (1996) 15–50.
- [49] M. Nolan, G. Watson, The surface dependence of CO adsorption on ceria, *J. Phys. Chem. B* 110 (2006) 16600–16606.
- [50] J. Perdew, K. Burke, M. Ernzerhof, Generalized gradient approximation made simple, *Phys. Rev. Lett.* 77 (1996) 3865–3868.
- [51] Y. Zhang, Y. Liu, L. Zhang, X.E.L. Pan, X. Zhang, A. Fazale, D. Zou, S. Liu, J. Zou, DFT study on water oxidation on nitrogen-doped ceria oxide, *Appl. Surf. Sci.* 452 (2018) 423–428.
- [52] Y. Guo, S. Mei, K. Yuan, D. Wang, H. Liu, C. Yan, Y. Zhang, Low-temperature CO₂ methanation over CeO₂-supported Ru single atoms, nanoclusters, and nanoparticles competitively tuned by strong metal-support interactions and H-spillover effect, *ACS Catal.* 8 (2018) 6203–6215.
- [53] G. Henkelman, H. Jonsson, Improved tangent estimate in the nudged elastic band method for finding minimum energy paths and saddle points, *J. Chem. Phys.* 113 (2000) 9978–9985.
- [54] G. Henkelman, B.P. Uberuaga, H. Jonsson, A climbing image nudged elastic band method for finding saddle points and minimum energy paths, *J. Chem. Phys.* 113 (2000) 9901–9904.
- [55] S. Liu, A. Zhao, Z. He, Y. Li, D. Bi, X. Gao, Effects of temperature and urea concentration on nitrogen-rich pyrolysis: Pyrolysis behavior and product distribution in bio-oil, *Energy* 239 (2022), 122443.
- [56] X. Lei, X. Xue, H. Yang, C. Chen, X. Li, M. Niu, X. Gao, Y. Yang, Effect of calcination temperature on the structure and visible-light photocatalytic activities of (N, S and C) co-doped TiO₂ nano-materials, *Appl. Surf. Sci.* 332 (2015) 172–180.
- [57] J. Marques, T. Gomes, M. Forte, R. Silva, C. Tavares, A new route for the synthesis of highly-active N-doped TiO₂ nanoparticles for visible light photocatalysis using urea as nitrogen precursor, *Catal. Today* 326 (2019) 36–45.
- [58] C. Mao, Y. Zhao, X. Qiu, J. Zhu, C. Burda, Synthesis, characterization and computational study of nitrogen-doped CeO₂ nanoparticles with visible-light activity, *Phys. Chem. Chem. Phys.* 10 (2008) 5633–5638.
- [59] A. Jorge, Y. Sakatani, C. Boissiere, C. Laberty-Roberts, G. Sauthier, J. Fraxedas, C. Sanchez, A. Fuertes, Nanocrystalline N-doped ceria porous thin films as efficient visible-active photocatalysts, *J. Mater. Chem.* 22 (2012) 3220–3226.
- [60] S. Xiao, O. Takai, Formation and evaluation of CeN thin films, *Thin Solid Films* 317 (1998) 137–139.
- [61] A. Jorge, J. Fraxedas, A. Cantarero, A. Williams, J. Rodgers, J. Attfield, A. Fuertes, Nitrogen doping of ceria, *Chem. Mater.* 20 (2008) 1682–1684.
- [62] J. Wang, D. Tafen, J. Lewis, Z. Hong, A. Manivannan, M. Zhi, M. Li, N. Wu, Origin of photocatalytic activity of Nitrogen-doped TiO₂ nanobelts, *J. Am. Chem. Soc.* 131 (2009) 12290–12297.
- [63] D. Guo, Z. Wan, Y. Li, B. Xi, C. Wang, TiN@Co_{5.47}N composite material constructed by atomic layer deposition as reliable electrocatalyst for oxygen evolution reaction, *Adv. Funct. Mater.* 31 (2021).
- [64] C. Wang, W. Lu, Q. Lai, P. Xu, H. Zhang, X. Li, A. TiN, nanorod array 3D hierarchical composite electrode for ultrahigh-power-density bromine-based flow batteries, *Adv. Mater.* 31 (2019).
- [65] W. Choi, C. Lee, H. Kim, S. Lee, J. Bang, Designing a high-performance nitrogen-doped titanium dioxide anode material for lithium-ion batteries by unravelling the nitrogen doping effect, *Nano Energy* 74 (2020), 104829.
- [66] Y. Zhang, F. Du, X. Yan, Y. Jin, K. Zhu, X. Wang, H. Li, G. Chen, C. Wang, Y. Wei, Improvements in the electrochemical kinetic properties and rate capability of anatase titanium dioxide nanoparticles by nitrogen doping, *ACS Appl. Mater. Interfaces* 6 (2014) 4458–4465.
- [67] J. Lee, S. Lee, J. Choung, C. Kim, K. Lee, Ag-incorporated macroporous CeO₂ catalysts for soot oxidation: Effects of Ag amount on the generation of active oxygen species, *Appl. Catal. B Environ.* 246 (2019) 356–366.
- [68] S. Tian, S. Zhan, Z. Lou, J. Zhu, J. Feng, Y. Xiong, Electrodeposition synthesis of 3D-NiO₁₋₈ flowers grown on Ni foam monolithic catalysts for efficient catalytic ozonation of VOCs, *J. Catal.* 398 (2021) 1–13.
- [69] L. Hao, H. Huang, Y. Zhang, T. Ma, Oxygen vacant semiconductor photocatalysts, *Adv. Funct. Mater.* 31 (2021) 2100919.
- [70] E. Brillas, I. Sires, M.A. Oturan, Electro-Fenton process and related electrochemical technologies based on Fenton's reaction chemistry, *Chem. Rev.* 109 (2009) 6570–6631.
- [71] G. Yu, Y. Wang, H. Cao, H. Zhao, Y. Xie, Reactive oxygen species and catalytic active sites in heterogeneous catalytic ozonation for water purification, *Environ. Sci. Technol.* 54 (2020) 5931–5946.